Unidirectional Bloch Modes for Low-Loss Contacted Microcavities

Jeffrey M. Shainline[1], Jason Orcutt[2], Mark T. Wade[1], Kareem Nammari[1], Ofer Tehar-Zahav[3], Zvi Sternberg[3], Roy Meade[4], Vladimir Stojanović[2] and Miloš Popović[1]

[1]*Department of Electrical, Computer and Energy Engineering, University of Colorado, Boulder, Colorado 80309, USA*
[2]*Research Laboratory of Electronics, Massachusetts Institute of Technology, 77 Massachusetts Ave, Cambridge, Massachusetts 02139, USA*
Massachusetts Ave, Cambridge, Massachusetts 02139, USA
[3]*Micron Semiconductor Israel, Kiryat-Gat, Israel*
[4]*Micron Technology, Inc. Process R&D, Boise, ID, USA*
jeffrey.shainline@osamember.org

http://plab.colorado.edu

Abstract: To access degrees of freedom of optical cavities, it is often advantageous to make material contact to the cavities themselves. We present a cavity design which enables large numbers of contacts (up to 62 in this work) to be placed in direct contact with waveguide sidewalls. By exciting a superposition of modes with a particular ratio of amplitudes, a spatial field pattern with periodic nodes along the sidewalls is established. We refer to this state as a Unidirectional Bloch Mode; contacts placed in the nulls of this mode introduce little scattering loss. Devices were fabricated by Micron Technology in a polysilicon DRAM process. We present measurements of racetrack-type optical cavities with as many as 62 silicon contacts. Quality factors are consistently measured to exceed 20,000. Accounting for the independently measured polysilicon loss of 10dB/cm, Q factors of 30,000 are consistently observed with peak values exceeding 40,000. Such Q factors are sufficient for many photonic applications including optoelectronics, optomechanics, and particle sensing. The large numbers of contacts give simultaneous access to electrical, mechanical, and thermal degrees of freedom.

OCIS codes: (230.5750) Resonators, (250.5300) Photonic integrated circuits, (130.3990) Micro-optical devices, (130.3120) Integrated optics devices

References and links

1. Q. Xu, B. Schmidt, J. Shakya, and M. Lipson, "High speed carrier injection 18 Gb/s silicon micro-ring electro-optic modulator,", presented at The 20th Annual Meeting of the IEEE Lasers and Electro-Optics Society, 2007.
2. M.R. Watts, "Adiabatic microring resonators," Opt. Lett. **35,** 3231–3233 (2010).
3. C.T. DeRose and M.R. Watts and D.C. Trotter and D.L. Luck and G.N. Nielson and R.W. Young, "Silicon microring modulator with integrated heater and temperature sensor for thermal control," paper CThJ3, presented at the Conference on Lasers and Electrooptics (CLEO), May 2010.
4. J. Chan, A.H. Safavi-Naeini, J.T. Hill, S. Meenehan, and O. Painter, "Optimized optomechanical crystal cavity with acoustic radiation shield," Appl. Phys. Lett. **101,** 081115, (2012).

5. M.A. Popović, E.P. Ippen and F.X. Kärtner, "Low-Loss Bloch Waves in Open Structures and Highly Compact, Efficient Si Waveguide-Crossing Arrays," presented at the 20th Annual Meeting of the IEEE Lasers and Electro-Optics Society (LEOS), Lake Buena Vista, Florida, Oct. 2007.
6. J. Shainline, G. Fernandes, Z. Liu, and J. Xu, "Broad tuning of whispering-gallery modes in silicon microdisks," Opt. Express **18,** 14345–14352 (2010).
7. A.H. Atabaki and A.A. Eftekhar and S. Yegnanarayanan and A. Adibi, "Novel micro-heater structure for low-power and fast photonic reconfiguration," paper CWP6, presented at the Conference on Lasers and Electrooptics (CLEO), May 2010.
8. C. Batten and A. Joshi and J. Orcutt and A. Khilo and B. Moss and C.W. Holzwarth and M.A. Popović and H. Li and H.I. Smith and J.L. Hoyt and F.X. Kärtner and R.J. Ram and V. Stojanović and K. Asanović, "Building many-core processor-to-DRAM networks with monolithic CMOS silicon photonics," IEEE Micro **PP,** 8-21, (2009).
9. J.S. Orcutt, B. Moss, C. Sun, J. Leu, M. Georgas, J. Shainline, E. Zgraggen, H. Li, J. Sun, M. Weaver, S. Urošević, M. Popović, R.J. Ram, and V. Stojanović, "Open foundry platform for high-performance electronic-photonic integration," œ**20,** 12222-12232, (2012).
10. X. Xiao, H. Xu, X. Li, Y. Hu, K. Xiong, Z. Li, T. Chu, Y. Yu, and J. Yu, "25 Gbit/s silicon microring modulator based on misalignment-tolerant interleaved PN junctions," œ**20,** 2507-2515, (2012).
11. A. Taflove and S.C. Hagness, *Computational Electrodynamics: The Finite-Difference Time-Domain Method* (Artech House Publishers, New York, 2005).
12. K.K. Tsia, S. Fathpour, and Bahram Jalali, "Energy harvesting in silicon wavelength converters," œ**14,** 12327-12333, (2006).
13. H.A. Haus and W. Huang, "Coupled-mode theory," Proc. IEEE **79,** 1505-1518, (1991).
14. M.A. Popović, "Milos' thesis," (2009).
15. M.A. Popović, "Please suggest a reference," (2130).
16. E.G. Neumann, IEE Proc. Part H, **129,** 278 (1982).
17. Y. Liu and M. Popović, "High-Q Contacted Circular Microcavities Based on Loss-Avoiding Supermode Fields," *submitted to Integrated Photonics Research*, 2013.

1. Introduction

Many photonic systems rely on optical cavities to store light and/or control the density of optical states. With the extensive interdisciplinary branching of photonic subfields and the burgeoning complexity of integrated photonic devices, technologies which enable access to degrees of freedom of the cavities—electrical, mechanical, thermal, etc.,—enable experimentation with and utilization of multiple coupled physical mechanisms. Several cavity designs have been introduced to deal with this challenge [1, 2, 3, 4]. Here we present a class of silicon photonic microstructures which superpose multiple guided modes to form interference patterns with nulls where contacts can be made. We demonstrate racetrack resonators with contacts made directly to the waveguide sidewalls in the same lithographic and etch steps that define the waveguiding structures. Cavities with 62 contacts are demonstrated with intrinsic Q factors across the C-band averaging higher than 33,000 with peak values over 40,000 and FSRs of 507GHz. Structures with 10 contacts and FSRs of 1.12THz are also shown to have intrinsic Qs higher than 40,000.

We anticipate utilizing such cavities for optical modulators in CMOS-to-DRAM optical interconnects [8, 9]; however other applications will be discussed throughout the text. In many CMOS and DRAM processes, a partial etch is not available, so the popular ridge modulator design [1, 12] is not feasible. In poly-gate CMOS processes, the polysilicon can be patterned above the body silicon to form a ridge waveguide, but this polysilicon is often quite lossy. Due to the gate oxide, this only allows carrier modulation in the body silicon layer of the waveguiding structure [9]. Such a cavity design gives rise to broad resonances with small mode shifts. It becomes advantageous to form contacts on optical cavities in a single silicon layer without the need for a partial etch.

To demonstrate the feasibility of this cavity for a microelectronics process, we partnered with Micron Technology, a manufacturer of DRAM, to fabricate optical cavities in a native DRAM polysilicon process in a 90nm fabrication node with one significant process modification: the polysilicon was grown on a 1.2μm oxide layer for low-index undercladding. In the next section we discuss the principles of design of these cavities, and in Sec. 3 we present optical spectra

of the fabricated cavities. We conclude in Sec. 4. Additional data and discussion are in the appendices.

2. Contacted cavity design

The central idea behind this multi-mode approach to contacted waveguiding structures is to generate combinations of two or more modes which interfere in space to form field nodes where the waveguide can be touched without incurring substantial optical loss. To this end, we seek appropriate waveguide widths to support the desired number of modes. For simplicity, we begin with the two TE modes of largest effective index of refraction. Figure 1(a) shows the effective index of refraction for the three lowest-order TE modes as a function of waveguide width for a 225 nm silicon waveguide in an oxide cladding environment. We see that the TE_3 mode emerges from the cutoff defined by the oxide cladding at widths of ~ 800 nm. To ensure the TE_3 mode is not excited and does not disturb the field pattern, we do not wish to utilize waveguides wider than this.

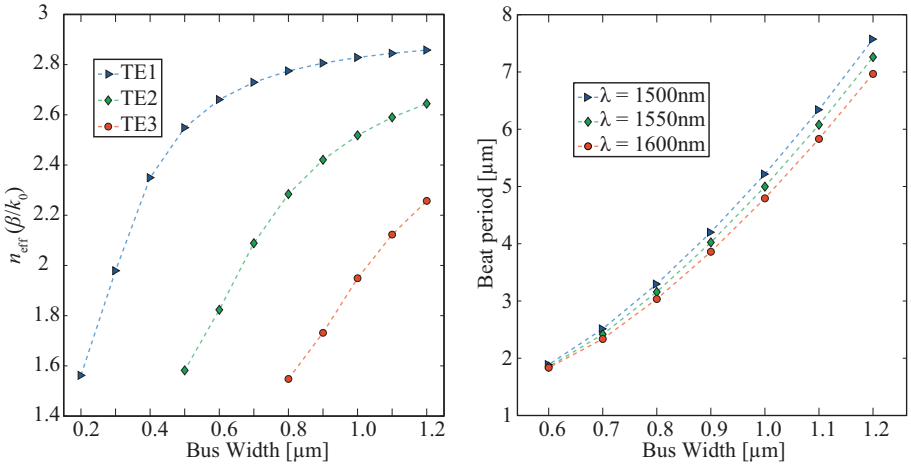

Fig. 1. (a) Effective indices of refraction ($n_{\text{eff}} = \beta/k_0$) for TE_1, TE_2, and TE_3 modes as a function of waveguide width. (b) Period of interference between modes TE_1 and TE_2 as a function of waveguide width for three wavelengths.

It also may be the case that a particular periodicity of contacts is suitable for a given application. Figure 1(b) shows the beat period, $\Lambda = 2\pi/(\beta_1 - \beta_2)$, as a function of waveguide width for three wavelengths. The similarity in beat periods over a 100nm wavelength range indicates the structures will have broad operating bandwidths, as we will see in Sec. 3. With the aim of designing a modulator consisting of two linear arms connected by 180° bends (a racetrack configuration) we desire longer periodicities so that the doped linear regions of the cavity constitute a greater fraction of the round trip length and therefore achieve a larger mode shift with voltage. To balance these constraints, we select an 800nm wide dual-mode waveguide width.

Investigating the performance of such dual-mode waveguides, we conduct FDTD [11] simulations in which a TE_1 mode is launched into a waveguide with contacts spaced at the interference period. In Fig. 2(a) we observe that after propagation through only a few contacts, the total field has formed into an interfering superposition of modes TE_1 and TE_2 which avoids the contacts. We can write the input field as

$$\bar{E}_i(\bar{r},t) = \bar{e}_1(\bar{r},t) \propto [a_1\bar{e}_1(\bar{r},t) + a_2\bar{e}_2(\bar{r},t)] + [a_1\bar{e}_1(\bar{r},t) - a_2\bar{e}_2(\bar{r},t)]. \quad (1)$$

This structure acts as a filter to eliminate the second term in the above expression for the initial field. To see this, we record the fields between each pair of adjacent contacts in the FDTD simulation and overlap them with the TE_1 and TE_2 modes to monitor the ratio $|a_1/a_2|^2$. The results of this calculation are shown in Fig. 2(b). Initially, all power is in the TE_1 mode, but the power in that mode quickly drops as the power in the TE_2 mode rises; the ratio of these two modes stabilizes as a function of contact index, and the total power loss per contact becomes quite low. The resulting low-loss optical mode is a unidirectional Bloch mode (UBM) arising from the superposition of two co-linearly propagating waveguide modes with differing propagation constants.

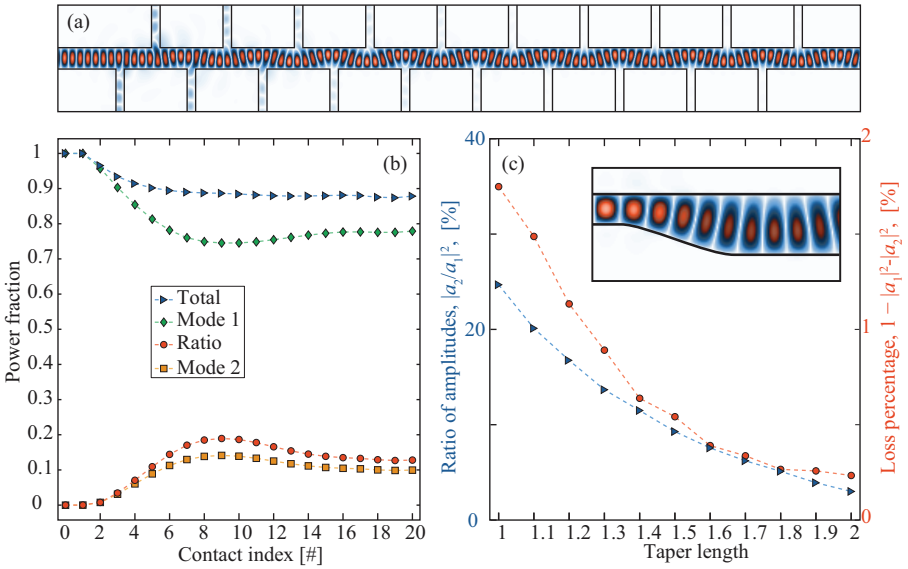

Fig. 2. (a) FDTD simulation of a TE_1 mode launched in an 800nm Si waveguide. The interference period between TE_1 and TE_2 in this structure is $\Lambda = 3.08\mu m$, and 10 periods of contacts have been placed with this periodicity. After propagation through several periods, it is evident that some energy has been transferred to the TE_2 mode, and the resulting field pattern avoids the contacts. (b) The power passing through a cross section between each pair of contacts has been observed. Power is transferred from TE_1 to TE_2, and this results in significantly reduced loss per contact. After propagating through all 10 periods, the ratio of amplitudes of modes TE_1 and TE_2 approaches a constant, and the low-loss UBM has been established. (c) By utilizing a non-adiabatic taper, the desired ratio of mode amplitudes can be excited. Here we plot the ratio of amplitudes as well as the loss as a function of taper length.

One would like to find a means to couple into the UBM by exciting the appropriate ratio of modes TE_1 and TE_2 without incurring the loss seen at the left of Fig. 2(b). Selective excitation of the two modes of differing symmetry is achieved with an asymmetric, non-adiabatic taper, as shown in the inset of Fig. 2(c). Figure 2(c) shows the ratio of the TE_1 and TE_2 modes excited as a function of taper length for a taper with sinusoidal transition shape from a single-mode waveguide of width 400nm to a dual mode width of 800nm. Having observed the optimal low-loss ratio present in the UBM, we now choose a taper length to excite this ratio. The location of the first field node along the sidewall can be approximated by analysis of the continuous-wave (CW) field pattern, as shown in the inset to Fig. 2(c), and the final parameters can be fine tuned in simulations of the complete structure. The chosen parameters for our designed structure are

listed in Table 1.

A CW simulation of excitation of and propagation through a completed UBM waveguide section is shown in Fig. 3(a). The taper exciteds a field which avoids even the first contact, and the intensity after the contact array is very nearly that at the input. An SEM image of the excitation taper and first few contacts is shown in Fig. 3(b). A microscope image of a UBM cavity with 10 periods on each arm is shown in Fig. 3(c). We now proceed to quantify light storage in these cavities.

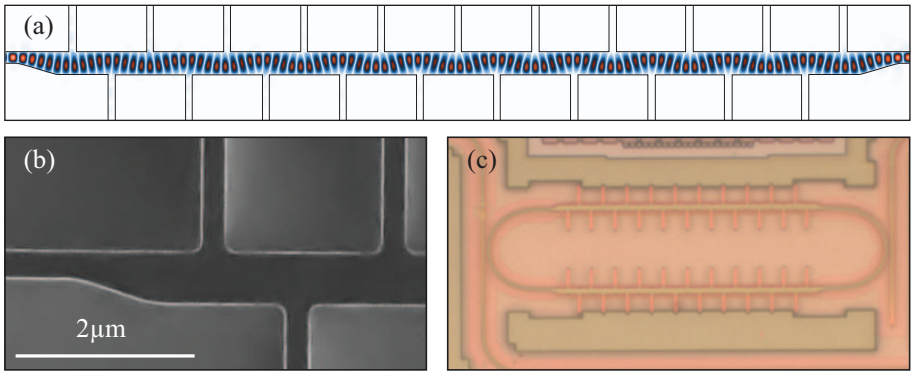

Fig. 3. (a) Light passes through an array of 21 contacts in a nearly lossless manner enabled by the excitation of a UBM. (b) An SEM image of a fabricated microcavity. An excitation taper as well as the first few contacts is shown. (c) A microscope image of a racetrack resonator with 42 contacts.

Table 1. Chosen parameters for UBM waveguiding structure utilizing TE_1 and TE_2. The first contact distance is measured from the end of the taper to the middle of the first contact.

Parameter	Value
Single mode width	400nm
Dual mode width	800nm
Contact period	3.08μm
Contact width	260nm
Taper length	1.86μm
First contact	560nm

3. Experimental results and analysis

We define the number of periods of contacts as N_Λ and the total number of contacts as N_{tot}; the total number of contacts on each resonator is $N_{\text{tot}} = 2(2N_\Lambda + 1)$. Devices with N_{tot} =10, 22, 34, 42 and 62 contacts (N_Λ =2, 5, 8, 10, and 15) were fabricated by Micron Technologies in a 225nm polysilicon layer with oxide over- and under-cladding using a 90nm DRAM foundry. The resonators are designed as described in Sec. 2 to operate at 1550nm, and the structure parameters are listed in Table 1. At 1550nm, the polysilicon propagation loss is near 10dB/cm and depends slightly on waveguide width. Q factors near the intrinsic values were experimentally ascertained with the loss ring method: several cavities of identical design are laid out along a common through port bus, and each cavity is coupled to an independent drop port of increasing ring/bus gap. For each device, the more-strongly-coupled ring/bus gaps are 290nm, and the weakly coupled gaps are 400nm. The coupling bus widths are 360nm. Qs are extracted for the

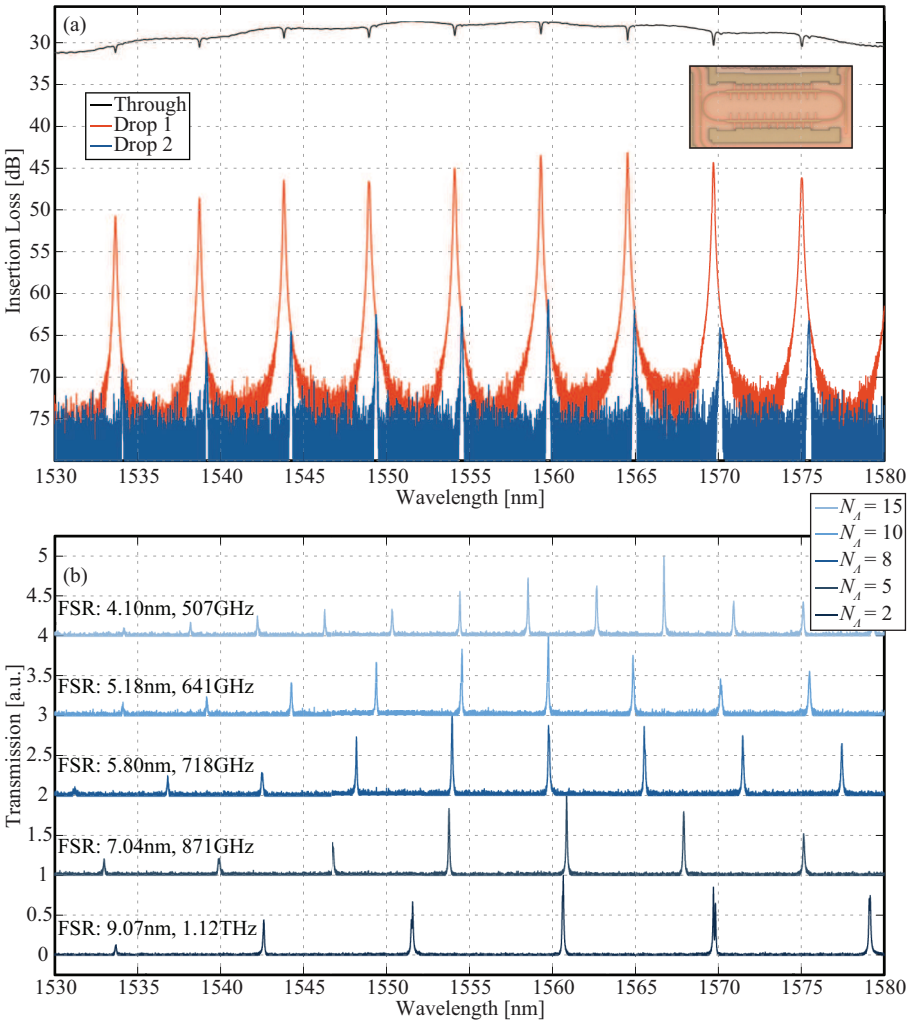

Fig. 4. (a) Spectra from a cavity with $N_\Lambda = 10$. A through port spectrum is shown, as well as a drop port spectrum from a structure with 290nm ring/bus gaps (drop 1), and a drop port with 400nm gaps (drop 2). (b) Spectra from the second drop port of cavities with $N_\Lambda = 2-15$.

least-loaded spectra which still rise sufficiently above the noise floor. Light is coupled onto and off of the chip with grating couplers [16]. Resonant wavelengths are measured with a swept laser in the through port, and this allows one to set the laser wavelength to a resonance to align a fiber to each cavity's drop port. Spectra from the through port as well as two drop ports of devices with $N_{\text{tot}} = 42$ are presented in Fig. 4(a) (cavity shown in inset). One can see that the through port is weakly coupled to the device with the smallest gaps and nearly uncoupled from the device with larger gaps. Correspondingly, the first drop port has considerably less noise, and the second drop port has Q factors that are more indicative of the intrinsic cavity Qs. The spectral response of the gratings gives rise to the envelope multiplying the heights of the peaks. The large number of resonances with well-defined FSR and similarity in linewidths (quantified in Table .1) demonstrates the wavelength-insensitivity of these devices.

Figure 4(b) shows spectra from the second drop port of structures with N_Λ =2, 5, 8, 10, and 15. All devices have high-Q resonances, and the FSR is determined by the number of periods as well as the length of the racetrack bends. Because straight-to-bend mode transitions have significant loss [17], we employ gradual racetrack bends with curvature that transitions from the straight waveguide section to that with a constant curvature. To help ensure losses are dominated by the UBM sections of the resonators, fairly large 5μm minimum radius-of-curvature gradual bends are utilized, and the length of each is $1.366\pi r_{\text{min}}$. To achieve larger FSRs, this radius could be reduced, and/or the geometry of the gradual bend could be improved.

Coupled mode theory is utilized to quantify the observed resonances. The model is presented in Appendix A. In the model for coupled counter-propagating modes, we find the resonances split in frequency as well as in Q factor. We refer to the greater of the two split Q factors as $Q_>$ and to the lesser as $Q_<$. In the present study, we find that nearly all resonances are better represented by the doublet model of Eqs. A2-A4 than the single-resonance model of Eq. A1. The resonances observed were quite consistent across the telecom C-Band with peak quality

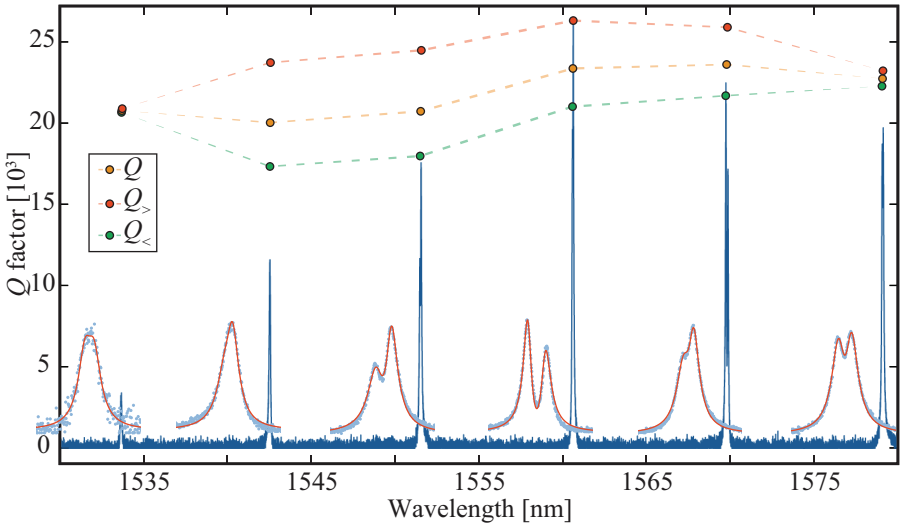

Fig. 5. Measured quality factors and resonance lineshape fits for each mode in the wavelength range 1530-1580nm of an $N_\Lambda = 2$ cavity.

factors near the designed frequency of operation. This is demonstrated in Fig. 5 where we show the Q factors of all resonances between 1530nm and 1580nm for an $N_\Lambda = 2$ cavity ($N_{\text{tot}} = 10$). The transmission spectrum is with respect to arbitrary linear units, and a magnified view of the region containing each resonance is shown at the base of each peak. While all resonances within this bandwidth have high Q factors, those near the target wavelength of operation are highest. In the case of this $N_\Lambda = 2$ cavity, the peak Q_t measured in this spectrum was $Q_t = 23,400$ with $Q_> = 26,300$. Accounting for the independently measured polysilicon propagation loss of 10dB/cm, this corresponds to a UBM-loss-limited cavity $Q_t^{\text{int}} = 35,300$ for the total loss Q, and $Q_>^{\text{int}} = 42,500$ for the higher-Q of the two split resonances.

The well-defined splitting in several of the resonances shown in Fig. 5 is clearly observed in cavities with $N_{\text{tot}} = 22$ as well, as is evidenced in Fig. 6. Figure 6(a) shows a microscope image of an $N_\Lambda = 5$ cavity. The spectrum from the first drop port is shown in Fig. 6(b). Doublet resonances are observed with $Q_> = 18,100$ which corresponds to an intrinsic $Q_>^{\text{int}} = 24,400$ in the absence of polysilicon propagation loss. One can see the excellent fit to a Lorentzian doublet.

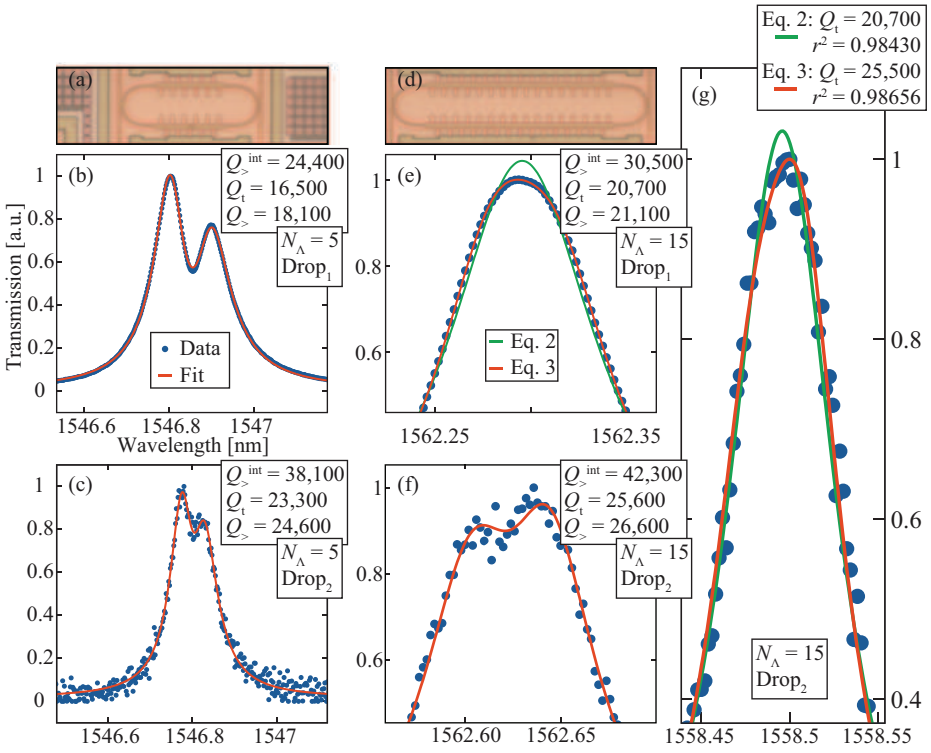

Fig. 6. (a)-(c) Data from an $N_\Lambda = 5$ cavity. (a) Microscope image of the cavity. (b) Close up view of the resonance with the highest value of Q_t in the device coupled to the first drop port. One sees the necessity of fitting to a doublet model. (c) The corresponding resonance of the device coupled to the second drop port. This resonance also has the highest value of Q_t of all resonances in the spectrum. While the mode splitting is reduced, the doublet model of Eqs. A2-A4 still provides an excellent fit to the measured data. (d)-(f) Data from an $N_\Lambda = 15$ cavity. (d) Microscope image of the cavity. (e) Close up of the resonance with the highest value of Q_t in the device coupled to the first drop port. Upon first glance, the data appear to have the shape of a single Lorentzian, like that in the singlet model of Eq. A1. However, comparison between the singlet and doublet models reveals the superior fit of the doublet model. The splitting is small compared to the linewidth, but quantitatively the passband is better fit to a narrowly split second-order system than the single Lorentzian of a first-order system. (f) The corresponding resonance in the device coupled to the second drop port. The doublet lineshape is quite evident. (g) Data of an adjacent resonance in the same spectrum as that shown in (e. Similar minimal splitting is observed, and again the doublet model provides an excellent fit to the peak of the resonance.

In Fig. 6(c) we see the corresponding resonance in the device on the second drop port with 400nm ring/bus gaps. While more noisy, the doublet resonance structure is quite evident; the measured Q factors are significantly higher: $Q_t = 23,300$ with $Q_> = 24,600$. In the absence of polysilicon loss, this corresponds to $Q_>^{\text{int}} = 38,100$.

Figure 6(d) shows an $N_\Lambda = 15$ cavity, and resonances from drop port one and two devices are shown in Figs. 6(e) and (f). The trends match those of the aforementioned cavities. With $N_{\text{tot}} = 62$, the splitting is not as apparent, but Figs. 6(e) and (g) show the discrepancy between the fits of the doublet model of Eq. A2-A4 and the single-lorentzian model of Eq. A1. Figures 6(e) and (g) display data from two different resonances to illustrate the consistency of the

observation, and in both cases the fit to a doublet model gives a higher r-squared value; the spectral fit of the model near the top of the passband is clearly more accurate with the doublet model. After accounting for the polysilicon loss, the doublet model gives $Q_t = 20,700$ and $Q_t^{\text{int}} = 30,500$ for the fit to this 290nm-gap drop port. For the 400nm drop port spectrum of Fig. 6(f), extracted intrinsic values are $Q_t^{\text{int}} = 40,700$ and $Q_>^{\text{int}} = 42,300$.

A more complete summary of the data is presented in Appendix B. Predicted and measured Qs of cavities with various numbers of periods is presented in Table B.1. A summary of the fit parameters which quantify the resonances in Fig. 6 is presented in Table B.2. It may seem counter-intuitive that cavities with a given number of contacts could have a comparable or even higher Q than a cavity with fewer contacts. The point is addressed in Appendix C.

One conclusion which we intend to emphasize with the breadth of data presented in Figs. 4-6 and Tables B.1 and B.2 is that UBMs present in these cavities are robust, and the cavities have a broad range of operation. Our results are not those of a few hero devices; rather they are present in each cavity across a broad range of frequencies, a broad range of values of N_Λ, and across a number of chips taken from various regions of the wafer.

4. Conclusions and outlook

Quality factors as high as those measured here are sufficient for many cavity applications including modulators, detectors, optomechanical structures, and nonlinear light-matter interactions. For such applications it is often necessary to access electrical, mechanical, or thermal degrees of freedom. An exceptional aspect of a cavity with 62 independently addressable contacts is that some can function to manipulate certain degrees of freedom leaving plenty for other uses, thus enabling highly multi-physical optical cavity systems.

While the present work has developed the racetrack geometry, it is worth noting that circular ring cavities making use of two whispering-gallery modes can form a more compact contacted cavity not requiring bends inaccessible by the contacts [18]. Alternatively, it is possible to make use of the fact that the mode is forced to the outer sidewall in the bending waveguide regions to place contacts on the inner sidewall in those regions, much like the work of Watts et al[2, 3]. This would allow the entire optical mode volume to be accessed by physical contacts, and the number and purpose of the independent contacts could be chosen for the application at hand.

Appendix A: Coupled mode theory of single and double resonances

To model the resonances observed in this work, we utilized Coupled Mode Theory in time (CMT)[14, 15]. The drop port response of a ring with one resonance is given by

$$\left|\frac{S_{3-}}{S_{1+}}\right|^2 = \frac{4r_o r_i}{\delta\omega^2 + r_t^2}. \tag{A1}$$

where $\delta\omega = \omega - \omega_0$. In Eq. A1, $r_t = r_i + r_o + r_l$; the total loss rate is the sum of the loss due to the input and output ports as well as all other losses, which are contained in r_l. The total cavity loss Q is given by $Q_t = \omega_0/2r_t$.

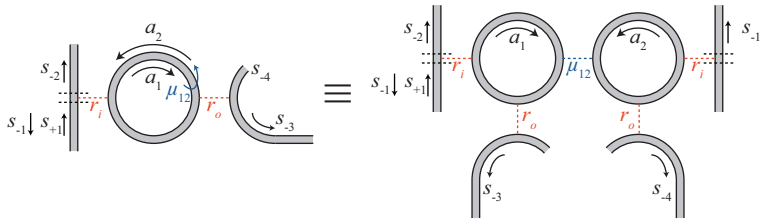

Fig. 7. Schematic of the ring/bus coupling model under consideration. The energy amplitudes of the two modes are a_1 and a_2; each oscillates with eigenfrequency ω_0 in the absence of coupling. The rate of input and output coupling to the bus waveguides are r_i and r_o, respectively. r_t represents other loss mechanisms. The linear coupling from mode one to mode two is represented by μ_{12}. The drop port amplitude is given by S_{3-}/S_{1+}.

In structures with sufficiently narrow linewidths, doublet resonances of two coupled counter-propagating modes are observed. A schematic of the configuration under consideration is shown in Fig. 7. On the left we show a representation of the counter-propagating modes of a single resonator. To elucidate the relation of the parameters to the CMT model, we map the system of two modes in a single cavity to the equivalent system of two cavities each with a single mode and a separate drop port. In this model, a_1 and a_2 are the energy amplitudes of two counter-propagating UBMs, and μ_{ij} is the linear coupling coefficient of mode i to mode j. We assume $\exp(-i\omega t)$ time dependence, so the measured drop port response of the coupled resonances is given by

$$\left|\frac{S_{3-}}{S_{1+}}\right|^2 = \left|\frac{-2\sqrt{r_o r_i}}{-i\delta\omega + r_t + \frac{\mu_{12}\mu_{21}}{-i\delta\omega + r_t}}\right|^2. \tag{A2}$$

The complex product $\mu_{12}\mu_{21}$ determines the magnitude and phase of the modal splitting. We write this product as $\mu_{12}\mu_{21} = |\mu_{12}\mu_{21}|\exp(i\angle\mu_{12}\mu_{21}) \equiv \mu^2\exp(i\phi_\mu)$. The CMT equations for the coupled counter-propagating modes in the absence of a through or drop port leads to an eigenvalue equation with eigenvalues corresponding to the split resonances of the system,

$$\omega_\pm = \omega_0 \pm \mu\cos(\frac{\phi_\mu}{2}) - i\left[r_t \mp \mu\sin(\frac{\phi_\mu}{2})\right], \tag{A3}$$

with corresponding split quality factors,

$$Q_\pm = \frac{-\mathrm{Re}(\omega_\pm)}{2\mathrm{Im}(\omega_\pm)} = \frac{\omega_0 \pm \mu\cos(\frac{\phi_\mu}{2})}{2\left[r_t \mp \mu\sin(\frac{\phi_\mu}{2})\right]}. \tag{A4}$$

The term $\mu\cos(\frac{\phi_\mu}{2})$ may be dropped in the numerator of Eq. A4 because it is much smaller than ω_0. Depending on the magnitude and phase of the splitting, it may be the case that either Q_+ or Q_- has a larger value. For the larger (smaller) of the two, we allocate the symbol $Q_>$ ($Q_<$).

Appendix B: Tabulated data

Here we present data from a number of different cavities. Table .1 shows a summary of resonances measured in cavities of $N_\Lambda = 2, 5, 8, 10$, and 15. Table .2 shows more detailed information on the resonances shown in Fig. 6.

Table .1. Measured Q values. For each entry, the Q values measured for each resonance in the spectral range from 1530nm to 1580nm were averaged to obtain $\bar{Q}$. $Q_{\max}$ denotes the largest of all measured and fit $Q_>$. σ is the standard deviation of that data set. $\bar{Q}^{\text{int}}$ is the average of the intrinsic Q factors of the same data set with the 10dB/cm polysilicon propagation loss accounted for. $\bar{r}^2$ is the average of coefficients of determination of the fits to the CMT model. $\mathscr{F}$ is the cavity finesse calculated using the measured FSR and $Q^{\text{int}}_{\max}$.

	$N_{\text{tot}} =$	10	22	34	42	62
Drop_1	$\bar{Q} =$	16,200	14,600	15,400	16,700	17,700
	$Q_{\max} =$	18,200	18,100	18,500	19,600	22,100
	$\sigma =$	1390	1760	1690	1820	2470
	$\bar{r}^2 =$	0.99981	0.99986	0.99966	0.99913	0.99980
$\text{Drop}_1^{\text{int}}$	$\bar{Q}^{\text{int}} =$	21,100	18,600	19,800	21,900	23,900
	$Q^{\text{int}}_{\max} =$	24,700	24,400	25,200	27,200	32,400
	$\sigma^{\text{int}} =$	1750	2620	2410	2540	4040
Drop_2	$\bar{Q} =$	22,000	19,900	19,900	20,000	22,900
	$Q_{max} =$	26,300	24,600	25,300	24,300	30,600
	$\sigma =$	2340	3260	2840	2990	3790
	$\bar{r}^2 =$	0.99980	0.97930	0.97548	0.94318	0.96683
$\text{Drop}_2^{\text{int}}$	$\bar{Q}^{\text{int}} =$	32,100	27,300	28,100	27,500	33,100
	$Q^{\text{int}}_{\max} =$	42,500	38,100	40,000	37,400	55,100
	$\sigma^{\text{int}} =$	3130	6010	4410	5510	6530
	$\mathscr{F} =$	249	173	150	125	146

Appendix C: Dependence of Q and finesse on N_Λ

As we have seen in this work, it can be the case that cavities with more contacts can have larger Q values. To see how this may arise, consider the relationship between Q and round-trip loss:

$$Q = \frac{20\pi n_g L}{\lambda_0 \ln(10) \mathrm{L}_{\text{dB/rt}}}. \tag{C1}$$

Here n_g is the group index, L is the total length of the cavity, and $\mathrm{L}_{\text{dB/rt}}$ is the loss in decibels per round trip. In Eq. C1, all factors are constant between cavities of differing N_Λ except the ratio $L/\mathrm{L}_{\text{dB/rt}}$. Thus, if the addition of another period of contacts brings more length than loss, it will raise the Q.

The round trip loss can be separated into a few components:

$$\mathrm{L}_{\text{dB/rt}} = 2\left(2\mathrm{L}_{\text{taper}} + \mathrm{L}_{\text{bend}} + \sum_{n=1}^{N_{\text{tot}}} \mathrm{L}_{\text{n}}\right). \tag{C2}$$

In this expression, the taper loss and the loss through the gradual bends are constant across cavities of differing N_Λ. We represent the loss due to the contacts as the sum over the loss at each contact to allow for the general case in which the loss varies down the length of the

Table .2. Parameters extracted from fits to the data shown in Fig. 6. All three Q values present in the model of Eqs. A2-A4 are listed, as well as the corresponding intrinsic estimates obtained by accounting for 10dB/cm polysilicon propagation loss, the r^2 values of the fits, and the resonance wavelength splitting, $\Delta\lambda$, measured in picometers.

	$N_{\text{tot}} =$	22	62
Drop_1	$Q_t =$	16,485	20,725
	$Q_t^{\text{int}} =$	21,593	29,624
	$Q_> =$	18,080	21,125
	$Q_>^{\text{int}} =$	24,415	30,447
	$Q_< =$	15,148	20,340
	$r^2 =$	0.99951	0.99988
	$\Delta\lambda =$	89.3	30.5
Drop_2	$Q_t =$	23,308	25,583
	$Q_t^{\text{int}} =$	35,023	40,666
	$Q_> =$	24,638	26,626
	$Q_>^{\text{int}} =$	38,114	42,316
	$Q_< =$	22,114	24,971
	$r^2 =$	0.98464	0.99037
	$\Delta\lambda =$	48.4	36.9
Eq. A1	$Q_t^{\text{sing}} =$		20,700
	$r^2 =$		0.98430
vs.			
Eq. A2	$Q_t^{\text{doub}} =$		24,500
	$r^2 =$		0.98656

structure. For example, the loss will vary as a function of contact index if a ratio other than the optimal UBM ratio is excited, or if the positioning of the first contact is slightly errant and the mode has to adjust it's phase.

The point here is that if L_n varies with n, it is most likely to be reduced with n. Thus, contacts at the beginning are likely to be slightly more lossy. Choosing well-informed values for the terms in the model of Eqs. C1 and C2, one can find sizeable regions of the parameter space where Q grows with N_Λ, and also where it does not. If the period of interference (which depends on wavelength) is slightly incommensurate with the period of the UBM, the loss per contact will outweigh the gain in length, and cavities with smaller N_Λ will have higher Q factors.

Perhaps it is also useful to consider the finesse. As we see in Table 1, the average Q value as a function of N_Λ is relatively constant. If we use this as our most indicative measure of Q, we conclude that the finesse is maximized in smaller N_Λ cavities where the FSR is maximized.